INTERNATIONAL JOURNAL FOR NUMERICAL METHODS IN ENGINEERING
*Int. J. Numer. Meth. Engng* (2007)
Published online in Wiley InterScience (www.interscience.wiley.com). DOI: 10.1002/nme.2192

# Lagrangian finite element treatment of transient vibration/acoustics of biosolids immersed in fluids

P. Krysl[1,*,†], T. W. Cranford[2] and J. A. Hildebrand[3]

[1]*University of California, San Diego, 9500 Gilman Dr. #0085, La Jolla, CA 92093-0085, U.S.A.*
[2]*San Diego State University, 5500 Campanile Dr., San Diego, CA 92182, U.S.A.*
[3]*Scripps Institution of Oceanography, University of California, San Diego, 9500 Gilman Dr. #0205, La Jolla, CA 92093-0205, U.S.A.*

SUMMARY

Superposition principle is used to separate the incident acoustic wave from the scattered and radiated waves in a displacement-based finite element model. An absorbing boundary condition is applied to the perturbation part of the displacement. Linear constitutive equation allows for inhomogeneous, anisotropic materials, both fluids and solids. Displacement-based finite elements are used for all materials in the computational volume. Robust performance for materials with limited compressibility is achieved using assumed-strain nodally integrated simplex elements or incompatible-mode brick elements. A centered-difference time-stepping algorithm is formulated to handle general damping accurately and efficiently. Verification problems (response of empty steel cylinder immersed in water to a step plane wave, and scattering of harmonic plane waves from an elastic sphere) are discussed for assumed-strain simplex and for voxel-based brick finite element models. A voxel-based modeling scheme for complex biological geometries is described, and two illustrative results are presented from the bioacoustics application domain: reception of sound by the human ear and simulation of biosonar in beaked whales. Copyright 2007 John Wiley & Sons, Ltd.

Received 30 April 2007; Revised 12 August 2007; Accepted 14 August 2007

KEY WORDS: bioacoustics; displacement-based finite element; human hearing; biosonar; beaked whale; acoustic wave; viscoelastic wave

## 1. INTRODUCTION

Models for the propagation of mechanical waves through biological specimens are becoming more widespread given significant recent advances in software and hardware. The challenges are many:

*Correspondence to: P. Krysl, University of California, San Diego, 9500 Gilman Dr. #0085, La Jolla, CA 92093-0085, U.S.A.
†E-mail: pkrysl@ucsd.edu

Contract/grant sponsor: U.S. Navy CNO-N45

heterogeneous, anisotropic, often only very slightly compressible, lossy (attenuating) materials; arbitrary mixtures of liquids and solids; complex geometries, with many features on multiple scales, requiring very large discrete models to achieve acceptable resolution; long propagation distances, with many wavelengths, and correspondingly long integration times. Considerable progress has been made in recent years: consult for instance References [1–8].

The present computational framework addresses all of the above aspects: Firstly, we formulate a displacement-based initial boundary value problem (IBVP) model using a superposition principle to separate the incident acoustic wave from the scattered and radiated waves. This novel use for the superposition as originally used in the scalar potential model by Sprague and Geers [9] allows the present model to handle arbitrary transient incident waves and multiple heterogeneous solid and fluid inclusions. To incorporate the effect of an infinite surrounding medium, an absorbing boundary condition, in this work in the form of the plane-wave approximation, is applied to the perturbation part of the displacement. The stress is assumed to depend linearly on the small-displacement, small-amplitude strain and strain rate, but we allow for inhomogeneous, anisotropic materials, both fluids and solids.

Secondly, we propose to discretize in space with displacement-based finite elements. Displacement-based finite elements have been used for fluids since early on [10, 11]. In some respects these formulations have proven tricky, especially when they produced non-zero (spurious) circulation modes or when they 'locked' for penalty rotational constraint in combination with models for almost incompressible fluids [12]. Various potential formulations have been proposed as remedies [13], or the displacement-based formulations have been converted to pressure/displacement ones [14]; literature on the subject is voluminous: refer for instance to Reference [9]. Nevertheless, several authors have shown that displacement-based finite elements can be used for fluids with good results if the capabilities of the elements are matched to the intended application [15–17]. In this work, we make use of two kinds of finite element formulations to treat fluids and solids with little compressibility robustly and efficiently: assumed-strain nodally integrated simplex elements and incompatible-mode brick elements. The unified treatment of fluids and solids allows for inhomogeneous, anisotropic materials, and simplifies the handling of fluid/solid interfaces which is normally difficult when different partial differential equation (PDE) models are used on the opposite sides of the interface.

Thirdly, we formulate a time-stepping algorithm to handle general damping accurately and efficiently. The transient nature of the problems we wish to address together with the very large size of the discrete system makes an explicit algorithm attractive (the centered differences being a natural candidate). However, the presence of damping couples the update equations [18, 19]. This makes the normally efficient update using a lumped (diagonal) system matrix (the mass matrix) potentially very expensive, as the system matrix will be a mixture of the mass matrix (diagonal) and the damping matrix (non-diagonal, in general). We formulate the centered-difference update in the classical form of an explicit Newmark to incorporate general damping using a fixed-point iteration solver, and we show that this solver achieves good efficiency provided the damping matrix due to the absorbing boundary conditions is reduced to a lumped (diagonal) form.

Finally, we describe our voxel-based modeling scheme for complex biological models. We introduce both verification (benchmark) problems (response of empty steel cylinder immersed in water to a step plane wave, and scattering of harmonic plane waves from an elastic sphere), and initial illustrative results from the bioacoustics application domain: reception of sound by the human ear and simulation of biosonar in beaked whales.



DOI: 10.1002/nme

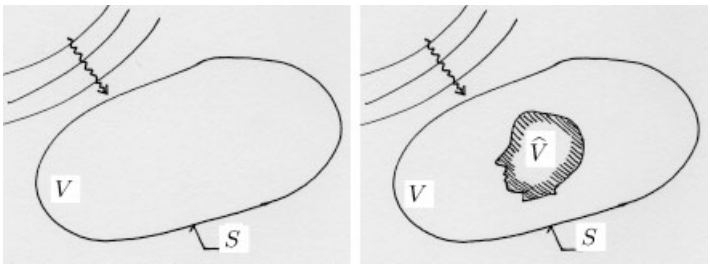


Figure 1. Train of waves passing through ideal fluid (left), and through a solid immersed in an ideal fluid (right).

## 2. DISPLACEMENT-BASED MODEL

Our goal is to compute the displacements and stresses in some object submerged in an infinite extent of ideal homogeneous fluid that are produced by an acoustic excitation that arrives through the fluid from some source either outside or inside the volume of interest.

First, consider an infinite extent of ideal fluid, with bulk modulus $K_W$, and mass density $_W$. Trace out an imaginary closed surface $S$, which contains a bounded volume of fluid $V$. Further, consider a train of waves passing through the fluid, traversing the volume $V$ (Figure 1). For certain kinds of waves, analytical solutions for the displacements of the particles of the fluid are available; for instance, for harmonic plane waves a displacement vector function may be written as

$$\mathbf{u}_{\text{inc}} = A\mathbf{n}\sin(\mathbf{n}\cdot\mathbf{r} - c_W t) \tag{1}$$

where $A$ is the amplitude, $\mathbf{n}$ is the normal to the plane of the wave, $c_W$ is the speed of sound in the fluid and $t$ is the time. From the known solution to the displacement field, it is possible to reconstruct the stress anywhere in the volume $V$ or on the surface $S$.

Now consider the original situation, in which the volume $V$ contains an inclusion $\widehat{V}$ which is not the same fluid, but rather a solid (for instance viscoelastic), or a different kind of fluid (viscous or inviscid). The waves that arrive from the source will be perturbed by the inclusion, and reflections and transmissions of waves will be generated. The wave pattern in the volume $V$ (the displacements of the fluid particles or of the solid particles) will not be available from analytical expressions such as (1). The goal of this section is to formulate a model to computationally solve for the displacement in the volume.

### *2.1. Displacement superposition*

We use displacement superposition as a basic tool to separate the effect of the forcing by the train of incident acoustic waves from the scattering and radiation due to the inclusion. The same principle has been used by Sprague and Geers [9], but for a pressure-based (scalar potential) formulation. The model will be formulated for the bounded volume $V$, incorporating the infinite extent of the fluid in the so-called absorbing boundary conditions.



DOI: 10.1002/nme

Thus, we write a standard weighted residual formulation of a small deformation, small strain Lagrangian deformation model [20]:

$$\int_V \boldsymbol{\eta}\cdot\ \ddot{\mathbf{u}}\,\mathrm{d}V-\int_V \boldsymbol{\eta}\cdot\overline{\mathbf{b}}\,\mathrm{d}V-\sum_{i=x,y,z}\int_{S_{t,i}}(\boldsymbol{\eta})_i\overline{t}_i\,\mathrm{d}S+\int_V(\mathscr{B}\boldsymbol{\eta})\cdot\boldsymbol{\sigma}\,\mathrm{d}V=0$$
$$u_i=\overline{u}_i\quad\text{and}\quad(\boldsymbol{\eta})_i=0\quad\text{on } S_{u,i}\quad\text{for } i=x,y,z \tag{2}$$

where $\boldsymbol{\eta}$ is the vector test function, $(\boldsymbol{\eta})_i$ indicates the $i$th component, $\mathbf{u}$ is the displacement vector function, $\overline{\mathbf{b}}$ is the known body load (for simplicity we may assume the body load to be absent, $\overline{\mathbf{b}}=\mathbf{0}$), $\overline{t}_i$ the $i$th component of the traction vector and $S_{t,i}$ is the part of the boundary $S$ on which the $i$th component of the traction is known. A discussion of the stress $\boldsymbol{\sigma}$ follows in Section 2.3. The displacements $\mathbf{u}$ and the test function $\boldsymbol{\eta}$ are assumed continuous across the inter-material interfaces; $\mathscr{B}$ is the symmetric gradient operator (produces the symmetrized small-deformation gradient tensor components, including a factor of two required for the shear components in the present 'Voigt' vector formulation [20]):

$$\mathscr{B}=\begin{bmatrix}\partial/\partial x & 0 & 0\\ 0 & \partial/\partial y & 0\\ 0 & 0 & \partial/\partial z\\ \partial/\partial y & \partial/\partial x & 0\\ \partial/\partial z & 0 & \partial/\partial x\\ 0 & \partial/\partial z & \partial/\partial y\end{bmatrix} \tag{3}$$

The integrals in (2) need to be evaluated over the volume of the fluid and the volume of each inclusion separately, but for simplicity we do not explicitly indicate that with notation. The mass density will assume different values depending on the material, $=\ _W$ in the surrounding fluid, $=\ _j$ for the $j$th inclusion.

### 2.2. Initial and boundary conditions

The IBVP requires the specification of the initial conditions at each point of $V$ at time $t=0$

$$\mathbf{u}(\mathbf{x},0)=\overline{\mathbf{W}}(\mathbf{x}),\quad \dot{\mathbf{u}}(\mathbf{x},0)=\overline{\mathbf{V}}(\mathbf{x}) \tag{4}$$

where $\overline{\mathbf{W}}(\mathbf{x})$ (the initial deflection) and $\overline{\mathbf{V}}(\mathbf{x})$ (the initial velocity) are known functions.

Now for the boundary conditions: On the surface $S$ we define any suitable Cartesian coordinate system at each point, and express the boundary conditions in terms of the components: $\overline{t}_i$ is a component of the traction vector prescribed on $S_{t,i}$, and $\overline{u}_i$ is a component of the displacement vector prescribed on $S_{u,i}$. In our case, the displacement components are not known on any part of the surface $S$, and the boundary conditions on $S$ will be developed entirely in terms of the tractions on that surface. Therefore,

$$S_{t,i}=S,\quad S_{u,i}=\emptyset\quad\text{for } i=x,y,z \tag{5}$$

It is not possible to construct a solution to the IBVP (2) with the initial conditions (4), because the boundary tractions are unknown. Initial progress is derived from the (usual) assumption that



DOI: 10.1002/nme

the surrounding fluid medium supports only normal stresses. Therefore, the traction vector on $S$ will have only the normal component

$$\mathbf{t} = -p_W \mathbf{n}$$

where $p_W = -(\ _x + \ _y + \ _z)/3$ is the pressure in the fluid, expressed through the normal components of the stress in the fluid, and $\mathbf{n}$ is the outward normal to $S$. The pressure in the fluid $p_W$ is unknown, but it is possible to separate the pressure on the surface $S$ into two constituents: the first part will be the pressure corresponding to the incident excitation wave (for instance, as generated by (1)), and therefore known; the second part will be everything else, in other words the perturbation due to the scattered and radiated waves produced by the inclusion(s). Thus, we will write the total pressure in the fluid as

$$p_W = p_{\text{inc}} + P$$

where $p_{\text{inc}}$ is known from the analytical solution, and $P$ is the pressure disturbance due to the inclusions.

The second advance in the formulation of the boundary conditions may be now made if we assume that the perturbation pressure is due to waves which will only pass through the surface $S$ from the volume $V$ to the exterior infinite part of the fluid domain (note that for this to work the bounding surface $S$ needs to be convex). The displacement may be decomposed as

$$\mathbf{u} = \mathbf{u}_{\text{inc}} + \mathbf{U}$$

where $\mathbf{u}_{\text{inc}}$ is the known analytical solution, and $\mathbf{U}$ is the displacement disturbance due to the inclusions. Now, if the pressure disturbance is produced only by the disturbance part of the displacement (which is a reasonable assumption for small-amplitude acoustic excitation in an ideal fluid), some form of an absorbing boundary condition may be invoked on $S$ [21–26].

For our particular range of applications, the early-time approximations [21, 27] are especially relevant, both the so-called plane-wave approximation [27] and the curved-wave approximation [28]. More accurate alternatives are available: The first-order doubly asymptotic approximation (DAA) [29] improves accuracy for low-frequency wave motion (late-time added mass effects). High-order DAA's and other sophisticated treatments of absorbing boundary conditions [22–26] may improve the accuracy, but the cost would tend to be significant. Thus, the trade-off is between accuracy (DAA more accurate than early-time approximations, curved-wave approximation more accurate than plane-wave approximation) and cost (DAA and curved-wave approximation more costly than plane-wave approximation). Owing to the transient nature of the expected applications, which will clearly require many repeated evaluations of the absorbing boundary condition, the cost associated with more accurate conditions may well be excessive. Therefore, the plane-wave approximation [21, 27] was adopted in this work

$$P = \ _W c_W \dot{\mathbf{U}} \cdot \mathbf{n} \tag{6}$$

to link the unknown perturbation pressure to the (still unknown) perturbation displacement. This is the time-dependent approximation of the Sommerfeld radiation condition for time harmonic pressure field at infinity (i.e. only outgoing waves are allowed to pass through the convex bounding surface as the bounding surface is moved to infinity in all directions). With the elimination of



DOI: 10.1002/nme

$P$ from the boundary condition the weighted residual statement becomes well defined, as upon substitution into (2) we obtain first

$$\int_V \boldsymbol{\eta}\cdot\ \ddot{\mathbf{u}}\,\mathrm{d}V-\int_S \boldsymbol{\eta}\cdot p_W\mathbf{n}\,\mathrm{d}S+\int_V (\mathscr{B}\boldsymbol{\eta})\cdot\boldsymbol{\sigma}\,\mathrm{d}V=0$$

and then with the displacement decomposition and with (6) we obtain

$$\int_V \boldsymbol{\eta}\cdot\ \ddot{\mathbf{u}}_{\mathrm{inc}}\,\mathrm{d}V+\int_V \boldsymbol{\eta}\cdot\ \ddot{\mathbf{U}}\,\mathrm{d}V-\int_S \boldsymbol{\eta}\cdot p_{\mathrm{inc}}\mathbf{n}\,\mathrm{d}S-\int_S \left(\ {}_W c_W\dot{\mathbf{U}}\cdot\mathbf{n}\right)\boldsymbol{\eta}\cdot\mathbf{n}\mathrm{d}S+\int_V (\mathscr{B}\boldsymbol{\eta})\cdot\boldsymbol{\sigma}\,\mathrm{d}V=0 \tag{7}$$

written in terms of the perturbation displacement $\mathbf{U}$ as the only unknown. Next, the relationship of the perturbation displacement and the total stress $\boldsymbol{\sigma}$ will be discussed.

### 2.3. Constitutive equation

The primary unknown in Equation (7) is the perturbation displacement, $\mathbf{U}$. In the present model we assume that the stress $\boldsymbol{\sigma}$ may also be separated using the principle of superposition. We shall assume a constitutive equation of the form

$$\boldsymbol{\sigma}=\mathbf{D}_s\boldsymbol{\varepsilon}+\mathbf{D}_V\dot{\boldsymbol{\varepsilon}}$$

where $\boldsymbol{\varepsilon}$ is the total strain vector, $\dot{\boldsymbol{\varepsilon}}$ is the total strain rate vector, $\mathbf{D}_s$ is the material stiffness matrix (symmetric and positive semi-definite—allowing for fluids with zero shear stiffness), and $\mathbf{D}_V$ is the material damping matrix (symmetric). The matrices $\mathbf{D}_s, \mathbf{D}_V$ are allowed to vary from point to point (inhomogeneous materials), but they do not depend on any other quantity in the problem. Note also that we are allowing for general anisotropic materials, with general strain-rate (damping) response.

Using the displacement superposition, which yields for the total strain and the total strain rate

$$\boldsymbol{\varepsilon}=\mathscr{B}\mathbf{u}_{\mathrm{inc}}+\mathscr{B}\mathbf{U},\quad \dot{\boldsymbol{\varepsilon}}=\mathscr{B}\dot{\mathbf{u}}_{\mathrm{inc}}+\mathscr{B}\dot{\mathbf{U}}$$

the last term in (7) may be therefore split into a couple of known incident-wave-produced terms

$$\int_V (\mathscr{B}\boldsymbol{\eta})\cdot\mathbf{D}_s\mathscr{B}\mathbf{u}_{\mathrm{inc}}\,\mathrm{d}V+\int_V (\mathscr{B}\boldsymbol{\eta})\cdot\mathbf{D}_V\mathscr{B}\dot{\mathbf{u}}_{\mathrm{inc}}\,\mathrm{d}V \tag{8}$$

and the perturbation–displacement terms

$$\int_V (\mathscr{B}\boldsymbol{\eta})\cdot\mathbf{D}_s\mathscr{B}\mathbf{U}\,\mathrm{d}V+\int_V (\mathscr{B}\boldsymbol{\eta})\cdot\mathbf{D}_V\mathscr{B}\dot{\mathbf{U}}\,\mathrm{d}V \tag{9}$$

The weighted residual statement (7) will become upon the incorporation of (8) and (9)

$$\begin{aligned}&\int_V \boldsymbol{\eta}\cdot\ \ddot{\mathbf{u}}_{\mathrm{inc}}\,\mathrm{d}V+\int_V \boldsymbol{\eta}\cdot\ \ddot{\mathbf{U}}\,\mathrm{d}V-\int_S \boldsymbol{\eta}\cdot p_{\mathrm{inc}}\mathbf{n}\,\mathrm{d}S-\int_S \left(\ {}_W c_W\dot{\mathbf{U}}\cdot\mathbf{n}\right)\boldsymbol{\eta}\cdot\mathbf{n}\,\mathrm{d}S\\&+\int_V (\mathscr{B}\boldsymbol{\eta})\cdot\mathbf{D}_s\mathscr{B}\mathbf{u}_{\mathrm{inc}}\,\mathrm{d}V+\int_V (\mathscr{B}\boldsymbol{\eta})\cdot\mathbf{D}_V\mathscr{B}\dot{\mathbf{u}}_{\mathrm{inc}}\,\mathrm{d}V\\&+\int_V (\mathscr{B}\boldsymbol{\eta})\cdot\mathbf{D}_s\mathscr{B}\mathbf{U}\,\mathrm{d}V+\int_V (\mathscr{B}\boldsymbol{\eta})\cdot\mathbf{D}_V\mathscr{B}\dot{\mathbf{U}}\,\mathrm{d}V=0\end{aligned} \tag{10}$$

entirely in terms of the single unknown field, the perturbation displacement $\mathbf{U}$.



DOI: 10.1002/nme

## 3. DIRECT TIME INTEGRATION

Upon standard spatial discretization of (10) with finite elements, the terms

$$\int_V \boldsymbol{\eta}\cdot\ \ddot{\mathbf{u}}_{\text{inc}}\,\mathrm{d}V - \int_S \boldsymbol{\eta}\cdot p_{\text{inc}}\mathbf{n}\,\mathrm{d}S + \int_V (\mathscr{B}\boldsymbol{\eta})\cdot\mathbf{D}_s\mathscr{B}\mathbf{u}_{\text{inc}}\,\mathrm{d}V + \int_V (\mathscr{B}\boldsymbol{\eta})\cdot\mathbf{D}_V\mathscr{B}\dot{\mathbf{u}}_{\text{inc}}\,\mathrm{d}V$$

will be an expression of the dynamic forces at the nodes due to the incident wave displacements. For convenience we avoid the surface integral by introducing an extended mesh: see Figure 2. The nodes on the boundary (the thick line) will be made *interior* to an extended mesh which is obtained by wrapping the domain mesh (shaded cells) with one layer of additional finite elements. The above terms will be therefore expressed in terms of (square) matrices computed for the extended mesh as

$$\mathbf{M}_{\text{ext}}\ddot{\mathbf{u}}_{\text{inc}} + \mathbf{C}_{\text{ext}}\dot{\mathbf{u}}_{\text{inc}} + \mathbf{K}_{\text{ext}}\mathbf{u}_{\text{inc}}$$

where we slightly abuse the notation by recycling the symbol $\mathbf{u}_{\text{inc}}$, formerly used for the incident displacement (vector with three component functions), for the column matrix representing the nodal parameters for the incident wave displacement. The matrices $\mathbf{M}_{\text{ext}}, \mathbf{C}_{\text{ext}}, \mathbf{K}_{\text{ext}}$ are never actually formed, the product is computed element by element.

The terms

$$\int_V \boldsymbol{\eta}\cdot\ \ddot{\mathbf{U}}\,\mathrm{d}V - \int_S (\ {}_W c_W\dot{\mathbf{U}}\cdot\mathbf{n})\boldsymbol{\eta}\cdot\mathbf{n}\,\mathrm{d}S + \int_V (\mathscr{B}\boldsymbol{\eta})\cdot\mathbf{D}_s\mathscr{B}\mathbf{U}\,\mathrm{d}V + \int_V (\mathscr{B}\boldsymbol{\eta})\cdot\mathbf{D}_V\mathscr{B}\dot{\mathbf{U}}\,\mathrm{d}V$$

will yield upon discretization

$$\mathbf{M}\ddot{\mathbf{U}} + (\mathbf{C}_{\text{ABC}} + \mathbf{C}_{\text{mat}})\dot{\mathbf{U}} + \mathbf{K}\mathbf{U} = \mathbf{M}\ddot{\mathbf{U}} + \mathbf{C}\dot{\mathbf{U}} + \mathbf{K}\mathbf{U}$$

where $\mathbf{U}$ represents the column matrix of the nodal parameters corresponding to the perturbation displacement, $\mathbf{M}$ and $\mathbf{K}$ are the mass and stiffness matrices, and $\mathbf{C}_{\text{ABC}}$ is the damping matrix

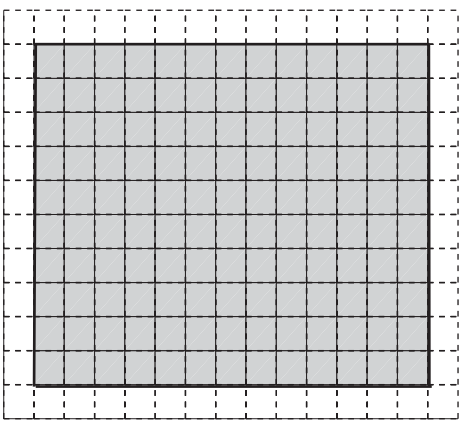

Figure 2. Mesh of the domain (shaded), mesh of the boundary of the domain (thick line), and the extended mesh (the shaded rectangles plus the empty cells on the circumference).



DOI: 10.1002/nme

resulting from the absorbing boundary condition, and $\mathbf{C}_{\text{mat}}$ is the material damping matrix. The coupled system of ordinary differential equations to be solved is therefore written as

$$\mathbf{M}\ddot{\mathbf{U}}+\mathbf{C}\dot{\mathbf{U}}+\mathbf{K}\mathbf{U}=-\mathbf{M}_{\text{ext}}\ddot{\mathbf{u}}_{\text{inc}}-\mathbf{C}_{\text{ext}}\dot{\mathbf{u}}_{\text{inc}}-\mathbf{K}_{\text{ext}}\mathbf{u}_{\text{inc}}$$

Next we will develop a suitable time-stepping procedure.

The centered-difference time-stepping algorithm may be formulated in several variants to accommodate general damping [19]. In this work, we apply the two-parameter Newmark algorithm as discussed in detail in Reference [20], substitute $=0$ to extract the explicit version (conditionally stable: time step must be shorter than the so-called critical time step which is related to the time taken by the fastest stress wave to traverse a single finite element [20]) and we arrive at the following algorithmic update equations:

$$\begin{aligned}\mathbf{U}_{t+\ t}&=\mathbf{U}_t+\ t\mathbf{V}_t+\frac{t^2}{2}\mathbf{A}_t\\ \mathbf{M}\mathbf{A}_{t+\ t}&=-\mathbf{K}\mathbf{U}_{t+\ t}-\mathbf{C}\mathbf{V}_{t+\ t}-\mathbf{r}_{\text{inc}}\\ \mathbf{V}_{t+\ t}&=\mathbf{V}_t+\frac{t}{2}(\mathbf{A}_t+\mathbf{A}_{t+\ t})\end{aligned}\tag{11}$$

where

$$\mathbf{r}_{\text{inc}}=\mathbf{K}_{\text{ext}}\mathbf{u}_{\text{inc},t+\ t}+\mathbf{C}_{\text{ext}}\mathbf{v}_{\text{inc},t+\ t}+\mathbf{M}_{\text{ext}}\mathbf{a}_{\text{inc},t+\ t}$$

If there is no damping ($\mathbf{C}=\mathbf{0}$, $\mathbf{C}_{\text{ext}}=\mathbf{0}$), the optimal efficiency of this algorithm derives from a diagonal (lumped) form of the mass matrix, since then the required linear system-of-equations solve in the second of the equations (11) is trivial.

Evidently, when damping is present (absorbing boundary condition is in effect, and/or materials exhibit damped response) the difficulty is that the update equations for the velocity $\mathbf{V}_{t+\ t}$ and the acceleration $\mathbf{A}_{t+\ t}$ in (11) are coupled. Substituting for the velocity from the last equation, the system of linear equations to be solved for $\mathbf{A}_{t+\ t}$ in each time step is

$$\left(\mathbf{M}+\frac{t}{2}\mathbf{C}\right)\mathbf{A}_{t+\ t}=\mathbf{r}_p\tag{12}$$

where

$$\mathbf{r}_p=-\mathbf{K}\mathbf{U}_{t+\ t}-\mathbf{C}\left(\mathbf{V}_t+\frac{t}{2}\mathbf{A}_t\right)-\mathbf{r}_{\text{inc}}$$

The system matrix for a general damping matrix $\mathbf{C}$ will be non-diagonal, and the solution of the system of equations may become an expensive operation, as pointed out for a different centered-difference formulation already by Park and Underwood [18]. These authors concluded that it was important to represent the general damping well for both accuracy and stability of the overall scheme, but at most two corrective iterations would be executed to minimize computational expense (which in their algorithm were not performed using the general damping matrix on the left-hand side).

Similarly, we find that the algorithmic update needs to be done consistently for both accuracy and stability reasons. Therefore, we attempt to solve (12) (a) accurately, while at the same time (b)



DOI: 10.1002/nme

minimizing the cost. One possible approach that avoids an expensive system-of-equations solve is to perform a few steps of fixed-point iteration

$$\mathbf{M}\mathbf{A}_{t+\ t}^{(k+1)} = \mathbf{r}_p - \frac{t}{2}\mathbf{C}\mathbf{A}_{t+\ t}^{(k)}, \quad k = 1, 2, \ldots \tag{13}$$

However, in the above form the convergence could be painfully slow. We will illustrate this with an example: Consider a model without material damping, in which case the damping matrix is only due to the absorbing boundary condition and rectangular 3-D finite element grid with spacing $x,\ y,\ z$. Using nodal integration will make the damping matrix diagonal with elements of the form

$$C_{jj} = \ _W c_W \ y \ z$$

for a node interior to the surface perpendicular to the $x$-axis, and analogously for the other two directions. The (diagonal) mass matrix element $jj$ would correspondingly be

$$M_{jj} = \tfrac{1}{2} \ _W \ x \ y \ z$$

Evaluating the expression for the iteration matrix $\mathbf{M}^{-1}(\ t/2)\mathbf{C}$, yields

$$\frac{t}{2} C_{jj}/M_{jj} = \frac{t c_W}{x}$$

Now, without loss of generality we can assume that $x$ is the shortest distance between nodes, and then we conclude that

$$\frac{t}{2} C_{jj}/M_{jj} = \frac{t}{t_{\mathrm{cr}}}$$

with the critical time step $t_{\mathrm{cr}} = x/c_W$. Since this fraction (which is the largest eigenvalue of the iteration matrix) may be arbitrarily close to one, we see that convergence of the fixed-point iteration could become very slow indeed.

To avoid this difficulty, we additively split the damping matrix

$$\mathbf{C} = \mathbf{C}_{\mathrm{ABC}} + \mathbf{C}_{\mathrm{mat}}$$

where $\mathbf{C}_{\mathrm{ABC}}$ is the damping matrix due to the absorbing boundary condition, and $\mathbf{C}_{\mathrm{mat}}$ is the material damping matrix. Furthermore, we form $\mathbf{C}_{\mathrm{ABC}}$ as a diagonal matrix. Then, the fixed-point iteration is started with the trivial solve (the system matrix is diagonal!)

$$\mathbf{A}_{t+\ t}^{(0)} = \left(\mathbf{M} + \frac{t}{2}\mathbf{C}_{\mathrm{ABC}}\right)^{-1} \mathbf{r}_p$$

followed by a few iterations of (13). Provided the sets of nodes affected by non-zero elements of $\mathbf{C}_{\mathrm{ABC}}$ and $\mathbf{C}_{\mathrm{mat}}$ are disjoint (such as when the material damping is only associated with the material of the inclusion), the predicted accelerations on the boundary are exact, and only the accelerations at interior nodes associated with material damping are iterated. For moderately weak damping the convergence is rapid; on the other hand, for strong damping iteration may be slow, and improvement of the iteration convergence by reduction of the time step then goes hand in hand with stability requirements (damping reduces the critical time step).



DOI: 10.1002/nme

## 4. BENCHMARK USING ASSUMED-STRAIN FINITE ELEMENTS

A good verification problem is the response of an infinitely long, air-filled, thin-walled steel cylinder submerged in water to a step plane-wave pressure pulse perpendicular to the axis of the cylinder. Various numerical solutions have been discussed for instance in References [30–36].

In this example we present results obtained on unstructured meshes. Simplex elements with nodal quadrature have been proposed in Reference [37] as an *ad hoc* technique based upon an averaged $B$ matrix as the strain–displacement operator (inspired by the well-known Flanagan, Belytschko formulas). Generalization of this work, using the Reissner strain–displacement principle to yield assumed-strain finite elements of other 1-, 2-, and 3-D shapes, has been recently developed [38].

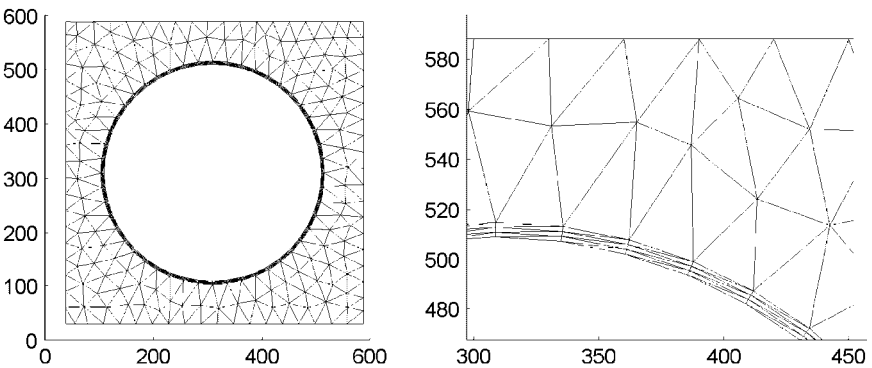


Figure 3. Mesh of the cylinder and the surrounding water. Domain size of $3R \times 3R$, mesh size $h = 30$.

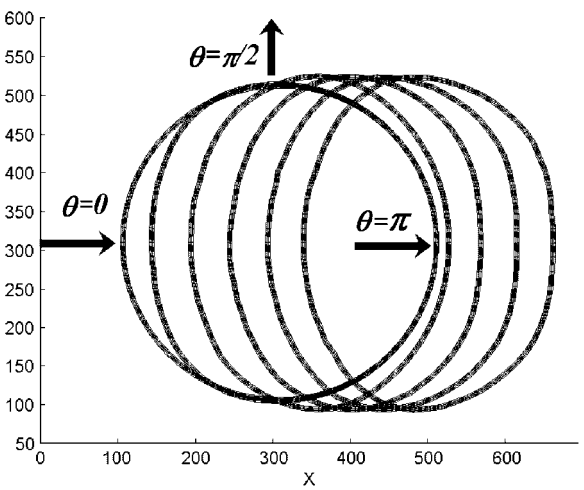


Figure 4. Shape of the cylinder at the time instants $tc/R = 0, 1, \ldots, 5$ ($c$ is the speed of sound in water).



DOI: 10.1002/nme

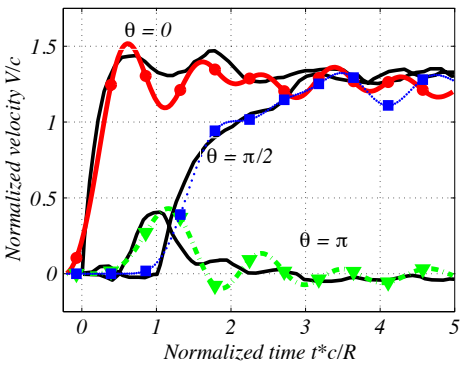


Figure 5. Normalized velocity $V/c$ of the points $=0$, $=\ /2$ and $=$ *versus* the normalized time $tc/R$. Domain size $4R \times 4R$, mesh size $h=30$.

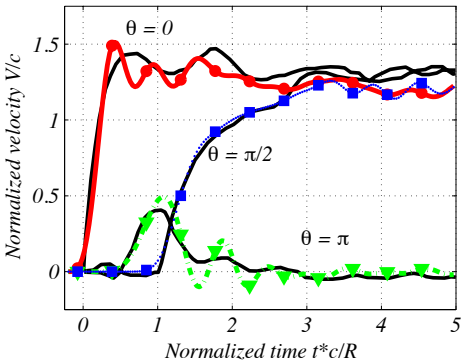


Figure 6. Normalized velocity $V/c$ of the points $=0$, $=\ /2$ and $=$ *versus* the normalized time $tc/R$. Domain size $3R \times 3R$, mesh size $h=15$.

The resulting finite elements are insensitive to volumetric locking due to reduced compressibility, their bending behavior is considerably improved, and they are relatively insensitive to aspect ratio [37]. We use a plane-strain model, with an unstructured uniform triangulation (three-nodes triangles) and the same type of approximation is used in the cylinder and in the surrounding water (Figure 3). We report results for two different mesh sizes. The coarsest mesh of the cylinder *(*$h=30$*)* is good enough to allow for the first five *in vacuo* free vibration modes to be computed within a 5% accuracy, despite the poor aspect ratio of the triangles in the mesh of the cylinder.

Huang has formulated a series solution based on modal expansion and the Laplace transform [30]. The solution for eight terms of the series is shown as a solid black line, and in the following figures serves as a reference. Figure 3 shows the mesh for the domain size $3R \times 3R$ ($R=205.9$ is the outer radius of the cylindrical shell), and mesh size $h=30$ (all in consistent units).

Figure 4 shows the magnified deformation of the cylinder at equally spaced time instants. The three points $=0$, $=\ /2$ and $=$ at the circumference of the steel cylinder at which velocities of the structure and pressures in the surrounding fluid are being measured are indicated with arrows.



DOI: 10.1002/nme

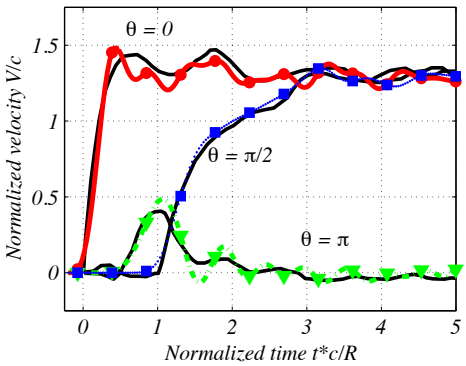


Figure 7. Normalized velocity $V/c$ of the points $=0$, $=\ /2$ and $=$ *versus* the normalized time $tc/R$. Domain size $4R \times 4R$, mesh size $h=15$.

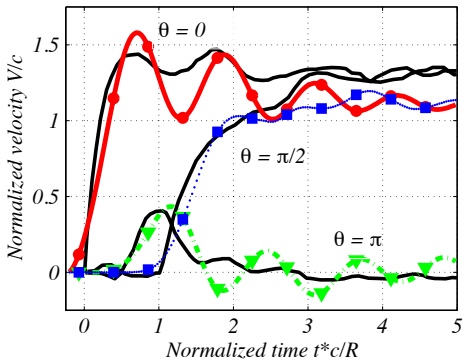


Figure 8. Normalized velocity $V/c$ of the points $=0$, $=\ /2$ and $=$ *versus* the normalized time $tc/R$. Domain size $3R \times 3R$, mesh size $h=30$.

Figure 8 shows the velocities of the three points $=0$, $=\ /2$, and $=$ for mesh size $h=30$, and domain size $3R \times 3R$ ($c$ is the speed of sound in water, $V$ is the magnitude of the velocity in the direction of the arrow). The present solution matches quite well in the early stages, but toward the end of the computational interval the speed attained by the cylinder in the direction of the pressure pulse is too low. This mismatch is likely due to the plane-wave approximation for the absorbing boundary (i.e. an early-time approximation). Increasing the size of the computational domain to $4R \times 4R$ leads to improved matching at the later stages (Figure 5). Similarly, for a finer mesh size, $h=15$, the computational domain $4R \times 4R$ improves the matching of the velocities compared with the domain size $3R \times 3R$: compare Figures 6 and 7.

## 5. VOXEL-BASED MODELING FOR BIOACOUSTICS

The starting points when modeling the geometry of biological specimens are usually volumetric images: CT, MRI and other scans. Using unstructured meshes for biological geometries poses



DOI: 10.1002/nme

many challenges. Not the least of them is the need to segment anatomical structures from which automatic mesh generation tools can produce volumetric and surface meshes. The latter step is fraught with difficulties of its own, and it is the subject of much research. The main point of having the mesh is to perform a vibration/acoustic analysis, in which the mesh serves as a means of approximating the mechanical behavior of the materials in the computational volume. The mechanical properties of the individual finite elements are nevertheless derived by mapping the information from the original volumetric images onto the mesh. An attractive alternative is to avoid this intermediate meshing step by using an image-based discrete model.

### *5.1. Generating the discrete model*

Modern volumetric image acquisition techniques produce three-dimensional data sets, typically as stacks of rectangular images. Therefore, it is quite natural to begin thinking in terms of the voxel tiling of the volume of interest. A voxel-based geometric representation of solids (volumes, in general) has a long history (refer, for instance, to the review [39]). Voxel meshes have also been utilized in computational procedures [5, 40, 41], including for wave propagation [42]. Voxel-based computations are rather appealing in that each voxel has an identical shape, which in turn may lead to considerable savings *via* pre-computation.

We describe our system for generating the discrete model next. The Analyze 7.5 volumetric image format has been adopted for both input data and for post-processing. An existing open-source Matlab toolkit has been adapted to provide the Analyze 7.5 volumetric image read/write capability. Various utilities have been developed to resample, resize and otherwise manipulate the volumetric data.

The intensity data of the 3-D images need to be mapped to material properties. To illustrate this procedure, we will use the example described previously for the head of the neonate Cuvier's beaked whale [43]. The animal's head was scanned with X-ray Computer Tomography (CT), as reported by Soldevilla *et al*. [44]. The data were collected continuously with 152 transverse scans along the longitudinal axis. The resolution within each transverse plane was 1.5 mm square pixels. Each of these transverse scans was 5 mm thick, collected every 5 mm. The GE Lightspeed scanner used a 500 mm diameter field of view scan region. The voxel values were in the Hounsfield units. All of the voxels external to the boundary of the head were converted to a Hounsfield value corresponding to seawater. Thus, the specimen was 'immersed' in an environment of sea water near sea-surface pressure. Additionally, a layer of water was wrapped around the specimen to ensure adequate space between the specimen and the bounding box for the simulations. In this case, approximately 30–80 mm was provided between the specimen and the bounding box. The voxel values in the Hounsfield units finally have been mapped to material density and other material parameters using a mapping given by Soldevilla *et al*. [44].

### *5.2. Finite element formulation*

Since all the elements are rectangular, the Wilson incompatible formulation is a natural choice: both the bending response and the dilatational locking insensitivity are significantly enhanced [20, 45]. No irrotationality constraint is used: its absence does not affect the quality of slosh and acoustic modes [17]. It does produce zero-frequency circulation modes which would be problematic for an eigenvalue solver, but that is not the case here.



DOI: 10.1002/nme

### *5.3. Implementation*

Matlab has been selected as the language of choice for the front-end of the simulation framework, with resulting portability and ease of use. The Matlab environment is used to develop simulation scripts, pre-process data, generate simulation source code and to post-process simulation results. The generated C-language source code is compiled on a suitable computer platform (Windows, Linux, or Mac OS-X workstation, Linux or IBM multiprocessor machines, etc.) The C-language source code for the finite elements simulation is generated automatically from templates to reflect the particulars of the study (input parameters, control parameters, etc.), and the various configuration options (double/single precision, computer platform, etc.). An important characteristic of the present framework is that the complete code for the simulation becomes an inseparable part of the simulation data, which guarantees repeatability and facilitates record keeping.

The compiled simulation is executed on the selected platform. The finite element code has been parallelized using pthreads (the POSIX thread mechanism for shared-memory multiprocessors). Because of the identical shape of the voxels, the strain–displacement operator may be computed just once for the entire mesh. Further optimization is achieved by binning materials: a finite number of material-type bins is created, typically a much smaller number of material types than there are cells, and all material-dependent calculations are precomputed for each material and then used over and over again when performing calculations on individual finite elements. A fairly high efficiency results. As an example, a Dell Precision 690 dual 3 GHz quad-CPU processor workstation can process a single element per CPU in approximately 5.7 s (for non-zero incident wave excitation; the computing time is approximately halved when the incident wave is absent).

Post-processing is performed again in Matlab, with various graphing and section-based visualization tools, and with volume rendering using the VTK toolkit [46].

### *5.4. Example: sound scattering from acoustically soft sphere*

In this example we present a numerical solution to a scattering problem. An elastic sphere is exposed to a train of planar harmonic waves in air (analytical solution available from Reference [47]). Sphere data: radius $R=0.0452\,\mathrm{m}$, mass density $\ _s=2000\,\mathrm{kg\,m^{-3}}$, Young's modulus $E_s=3\,\mathrm{GPa}$, Poisson ratio $\ _s=0.3$. Air data: mass density $\ _a=1.2\,\mathrm{kg\,m^{-3}}$, speed of sound $c_a=340\,\mathrm{m\,s^{-1}}$. The primary sound speed in the sphere is about 3.28 times higher than $c_a$. The acoustic forcing is a plane pressure wave of frequency $f=3\,\mathrm{kHz}$, which yields $k_aR\approx 2.5$ or $R/\ _a\approx 0.4$ ($k_a=2\ f/c_a$ is the wavenumber, $\ _a$ is the wavelength).

The harmonic incident plane wave is windowed with a hyperbolic-tangent time function to simulate a progressive wave. The arrival of the wave is illustrated in Figure 9: the five snapshots document the progression of the wave within one oscillation period. Within a few more oscillation cycles the pressure field around the sphere assumes the steady-state form.

The transient solution yields curves of pressure *versus* time at various points around the circumference. The ratio of the numerically integrated areas under one half wave of the computed response and the corresponding area under one half wave of the incident pressure approximates the pressure amplitude distribution.

Figure 10 shows the normalized total pressure amplitude around an elastic sphere for a plane wave propagating along the natural direction of the grid $\mathbf{n}=[1,0,0]$. The boundary is offset by $\ R$, where in this case $\ =\frac{1}{2}$. For $N_R=12$ elements along the radius of the sphere the approximation of the actual spherical surface is rather crude: see Figure 9, where in a darker shade overlay is a cross-section of the sphere. Still, the computed solution converges toward the analytical distribution



DOI: 10.1002/nme

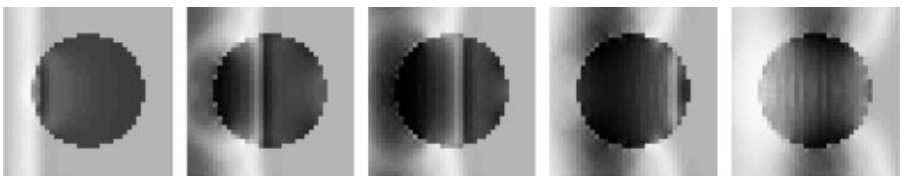

Figure 9. Normalized total pressure around a sphere. Boundary offset $=\frac{1}{2}$. Number of elements along the radius of the sphere $N_R=12$. Plane wave propagates in the direction $\mathbf{n}=[1,0,0]$. Grid for the sphere indicated with darker shade overlay. Positive pressures are light gray, negative pressures are dark gray.

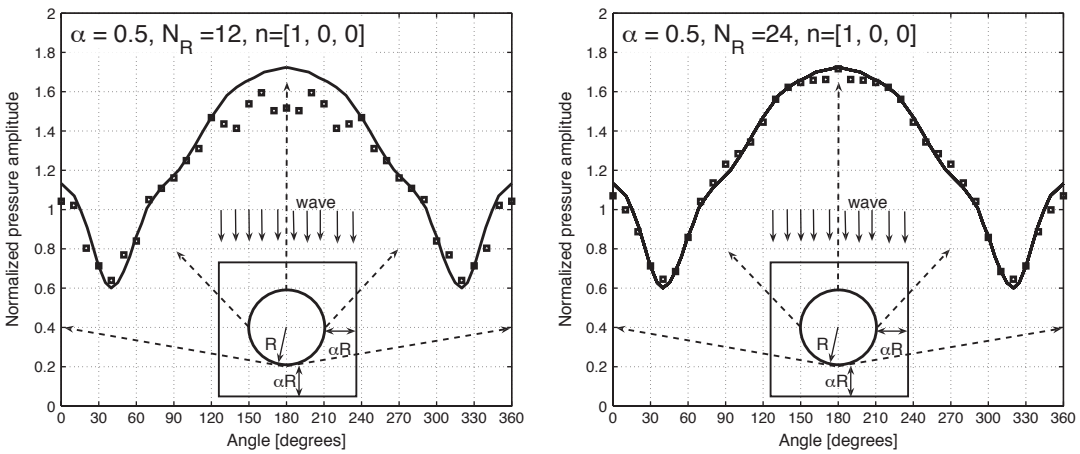


Figure 10. Normalized total pressure around a sphere. Boundary offset: $=1/2$ (refer to the inset). Number of elements along the radius of the sphere $N_R$. Plane wave propagates in the direction $\mathbf{n}=[1,0,0]$. Comparison with analytical deformable-sphere sound pressure solution.

for a stiff deformable sphere with mesh refinement, and thus one of the main requirements for the usability of the present technique is satisfied.

For practical applications it is important to recover essentially the same solution irrespectively of the direction of the incident wave. The present method displays a decent lack of sensitivity to the grid orientation as illustrated in Figure 11, which shows the normalized total pressure amplitude around an elastic sphere for a plane wave propagating along the direction $\mathbf{n}=[1,2,3]$. This wavefront direction breaks the symmetry of the grid. (The boundary is offset by the same amount $R$, with $=\frac{1}{2}$, as in the previous simulation.) The computed results show slight asymmetry, but qualitatively and quantitatively there is little difference with respect to Figure 10.

### *5.5. Example: simulation of received sound pressure level in humans*

We developed an acoustic wave propagation model to track and quantify an airborne incident acoustic wave in and around the human head. (Such models are of significant interest: For instance, alternate acoustic propagation paths into the inner ear can be investigated computationally, and the sound pressure amplitudes can be quantified [48].)



DOI: 10.1002/nme

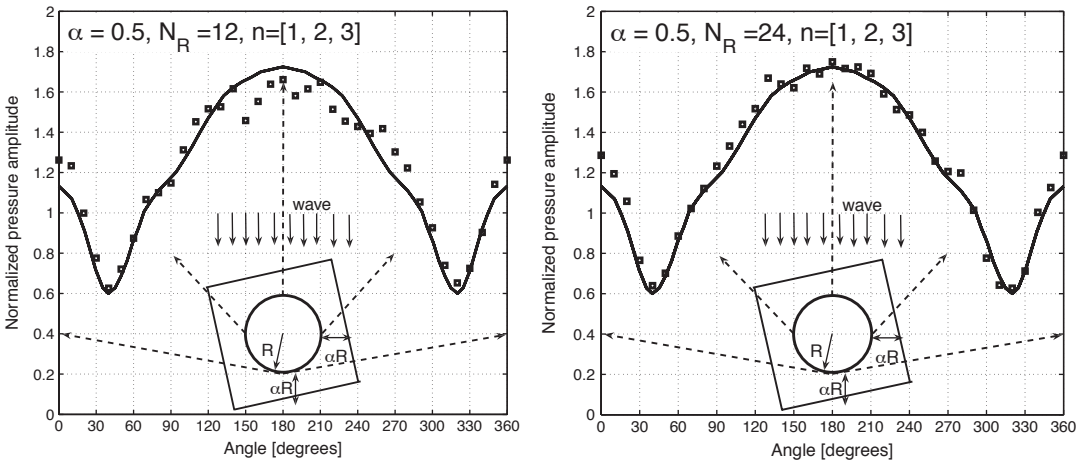


Figure 11. Normalized total pressure around a sphere. Boundary offset: $=\frac{1}{2}$ (refer to the inset). Number of elements along the radius of the sphere $N_R$. Plane wave propagates in the direction $\mathbf{n}=[1,2,3]$. Comparison with analytical deformable-sphere sound pressure solution.

We have adopted the 3-D CT scan of a human head publicly available on the web (University of Erlangen-Nürnberg), which is provided as unsigned eight-bit $512\times512\times106$ intensity data with resolution $0.436\,\mathrm{mm}\times0.436\,\mathrm{mm}\times2\,\mathrm{mm}$. The data set has been re-interpolated in the axial direction to yield the final data size of $512\times512\times504$ voxels, which is converted into a finite element model with over 132 million elements. The intensity data have been mapped to air (compressible inviscid fluid, sound speed $340\,\mathrm{m\,s^{-1}}$, $=1.2\,\mathrm{kg\,m^{-3}}$), tissue (slightly compressible isotropic solid, $E=0.25\,\mathrm{MPa}$, $=0.4999$, $=1100\,\mathrm{kg\,m^{-3}}$) and bone (isotropic solid, $E=2500\,\mathrm{MPa}$, $=0.22$, $=2000\,\mathrm{kg\,m^{-3}}$).

Using this data set, we have simulated the propagation of progressive plane harmonic waves of frequencies 3 and 20 kHz past the entire human head, and we have recorded the instantaneous acoustic pressure waveforms at various positions. Figure 12 shows a snapshot of the instantaneous pressure distribution for the 3 kHz excitation on one axial and one coronal section (light shades are high positive pressures; dark shades are high negative pressures); Figure 13 is a volume-rendered visualization of the pressure for the 20 kHz progressive-wave signal which has arrived roughly at the midsagittal plane (soft tissues are suppressed in the display, but were part of the model).

The pressure waveforms have been processed to extract approximate sound pressure levels. For 3 kHz, the sound pressure level received at the proximal eardrum is about 10.2 dB higher compared with the incident pressure level; for 20 kHz, the sound pressure level received at the proximal eardrum is about 6.6 dB lower than the incident pressure. These data agree reasonably well with published estimates of sound pressure level increase for the lowest resonance (around 3 kHz for adults) and of sound pressure level decrease at very high frequencies [49, 50].

Owing to its ability to deal with complex geometries, almost incompressible materials, and arbitrary transient incident waves, the present model seems to be well matched to investigations of some important questions in human hearing, for instance, the issue of bone conduction [51–54].



DOI: 10.1002/nme

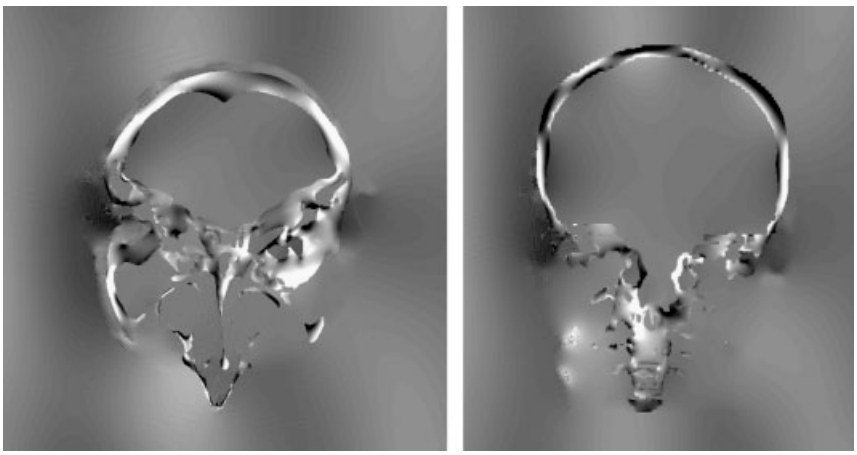

Figure 12. Planar section rendering of the total pressure in and around a human head. High positive pressure rendered in light shades and high negative pressure rendered in dark shades. Plane-wave excitation of 3 kHz. Grid with $512 \times 512 \times 504$ voxels.

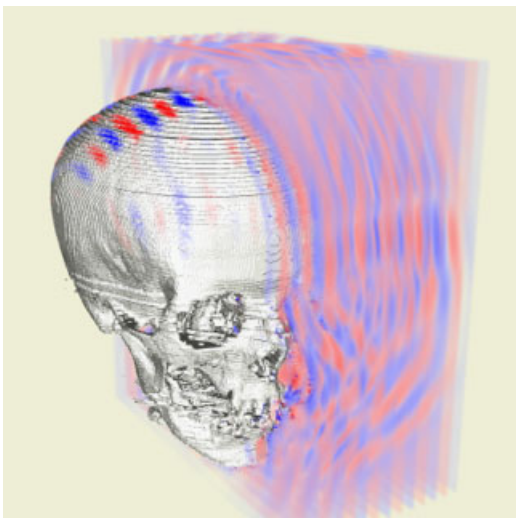

Figure 13. Volume rendering of the total pressure in and around a human head. High positive pressure is red and higher negative pressure rendered in blue. Plane-wave excitation of 20 kHz (the wavefront has just reached the mid-sagittal plane). The soft tissues are included in the calculation, but suppressed in the display. Grid with $512 \times 512 \times 504$ voxels.

### *5.6. Example: biosonar of beaked whales*

As awareness of noise pollution in the oceans increases, so does our interest in understanding hearing and sound production in marine vertebrates. Simulations are a powerful tool for



DOI: 10.1002/nme

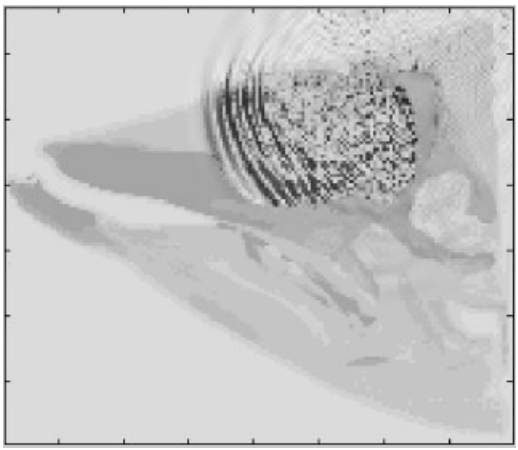

Figure 14. Pressure pulse generated by an echolocation click: distribution of pressure when the pressure pulse traversed the mid-section of the melon. High positive pressure is indicated by a dark color. The anatomy is displayed as shadows in the background.

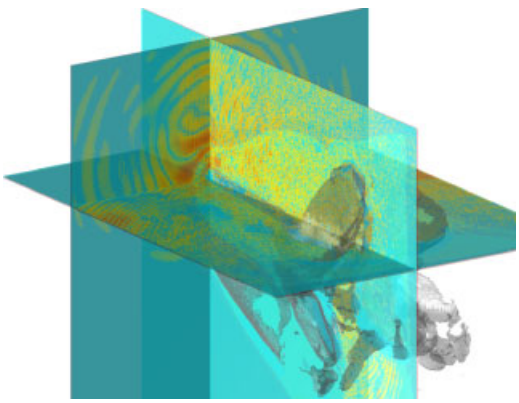

Figure 15. Pressure pulse generated by a click: distribution of acoustic intensity when the pressure pulse reached the nose of the animal. The bones of the skull are displayed as a semi-transparent surface.

investigating these effects in animals which are difficult to observe in nature, or for rapid explorations of ideas and hypotheses [43, 55].

The manner in which echolocation signals are produced by beaked whales is a matter of conjecture at this point. Here we report some preliminary results for simulations of echolocation click production in an adult beaked whale, *Ziphius cavirostris*.

The computational grid used in this study was a factor-two sub-sampling of the original CT scan which resulted in $247 \times 288 \times 332$ voxels, with the spatial resolution of the grid of $(3\,\mathrm{mm})^3$. The CT image intensity values have been used to assign one of nine materials to each voxel: air cavity, fatty tissues, muscle, connective tissue, soft bone, hard bone and porcelaineous bone. Tissue properties have not been measured for this specimen, but estimates were available from a specimen



DOI: 10.1002/nme

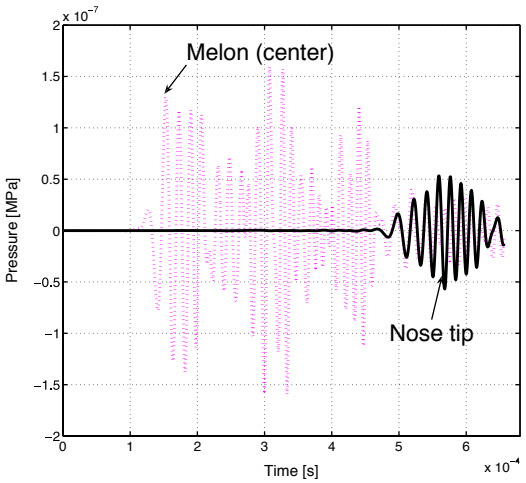


Figure 16. Pressure pulse generated by an echolocation click: pressure recorded in two locations within the anatomy.

of a neonate *Z. cavirostris* which was subjected to CT scans and tissue property measurements, reported by Soldevilla *et al*. [44].

The pressure pulse was produced by assigning non-zero initial bell-shaped radial velocity distribution to a small spherical volume (radius 10 mm) at the location of the phonic lips on the right side of the nasal apparatus.

Figure 14 shows the pressure distribution after the click disturbance traversed the mid-section of the melon (fatty body with some presumed acoustic function). The formation of a beam is clearly visible. This is also confirmed by Figure 15, where it is possible to identify a cone of high-intensity sound in a horizontal plane along the animal's nose. The filtering of the signal by the anatomy may be appreciated in Figure 16, which shows a complex signal recorded at the center of the melon, and a much cleaner wavelet recorded when the signal left the tissue of the animal at the top of its nose. An attempt to correlate these results with signals recorded by Zimmer *et al*. [56], with measurements of acoustic radiation by the harbor porpoises reported by Au *et al*. [57], and with signals produced by bottlenosed dolphins, is underway.

## 6. CONCLUSIONS

A displacement-based elasto-dynamic model using a superposition principle to separate the incident acoustic wave from the scattered and radiated waves has been formulated for complex biosolids (possibly with fluid inclusions) immersed in a fluid environment. An absorbing boundary condition is applied to the perturbation part of the displacement on the boundary of the computational domain to allow outgoing-only perturbation waves. The stress is assumed to depend linearly on the small-displacement, small-amplitude strain and strain rate, but we allow for inhomogeneous, anisotropic materials, both fluids and solids. The discrete model is obtained spatially with displacement-based finite elements (assumed-strain nodally integrated simplex elements and incompatible-mode brick elements) and temporally using a centered-difference time-stepping algorithm with a specialized



DOI: 10.1002/nme

solver of the resulting system of coupled equations to handle general damping accurately and efficiently. Both verification (benchmark) problems and illustrative results from the bioacoustics application domain have been discussed.

The present model has been developed with acoustics of hearing and sound production in mind. Investigations of sound reception and sound generation in marine mammals are ongoing, and the detailed results will be reported elsewhere.

On a parallel track is the use of the present acoustic wave propagation model to simulate acoustic waves around and inside the human head, which is of considerable medical and scientific interest [48]. The present model seems to be well suited to investigations of some important questions in human hearing, for instance the issue of bone conduction [51–54].

Large-scale simulation of ultrasonic pulse propagation for inhomogeneous tissue is becoming indispensable for the study of ultrasound-tissue interaction as well as for the development of new imaging methods. The concept of model-based imaging makes it possible to integrate structural and functional information [4, 5, 58, 59]. The present model can be integrated into coupled models used in estimations of ultrasound heating rates and other ultrasonic and biophysical effects [60].

## REFERENCES


1. Wojcik Jr G, Mould J, Lizzi F, Abboud N, Ostromogilsky M, Vaughan D. Nonlinear modeling of therapeutic ultrasound. *IEEE Ultrasonics Symposium Proceedings*, Seattle, WA, 1995.
2. Wojcik G, Fornberg B, Waag R, Carcione L, Mould J, Nikodym L, Driscoll T. Pseudospectral methods for large-scale bioacoustic models. *1997 Ultrasonics Symposium Proceedings*, Ontario, Canada, 1997.
3. Mast TD, Hinkelman LM, Orr MJ, Sparrow VW, Waag RC. Simulation of ultrasonic pulse propagation through the abdominal wall. *Journal of the Acoustical Society of America* 1997; **102**(2):1177–1190.
4. Mast TD, Hinkelman LM, Orr MJ, Waag RC. The effect of abdominal wall morphology on ultrasonic pulse distortion. Part ii. Simulations. *Journal of the Acoustical Society of America* 1998; **104**(6):3651–3664.
5. Mast TD, Hinkelman LM, Metlay LA, Orr MJ, Waag RC. Simulation of ultrasonic pulse propagation, distortion, and attenuation in the human chest wall. *Journal of the Acoustical Society of America* 1999; **106**(6):3665–3677.
6. Mast TD, Souriau LP, Liu DLD, Tabei M, Nachman AI, Waag RC. A kappa-space method for large-scale models of wave propagation in tissue. *IEEE Transactions on Ultrasonics Ferroelectrics and Frequency Control* 2001; **48**(2):341–354.
7. Tabei M, Mast TD, Waag RC. A *k*-space method for coupled first-order acoustic propagation equations. *Journal of the Acoustical Society of America* 2002; **111**(1):53–63.
8. Varslot T, Taraldsen G. Computer simulation of forward wave propagation in soft tissue. *IEEE Transactions on Ultrasonics Ferroelectrics and Frequency Control* 2005; **52**(9):1473–1482.
9. Sprague MA, Geers TL. Spectral elements and field separation for an acoustic fluid subject to cavitation. *Journal of Computational Physics* 2003; **184**(1):149–162.
10. Belytschko T. Methods and programs for analysis of fluid–structure systems. *Nuclear Engineering and Design* 1977; **42**(1):41–52.
11. Bathe KJ, Hahn WF. Transient analysis of fluid–structure systems. *Computers and Structures* 1979; **10**(1–2): 383–391.
12. Olson LG, Bathe KJ. A study of displacement-based fluid finite-elements for calculating frequencies of fluid and fluid structure systems. *Nuclear Engineering and Design* 1983; **76**(2):137–151.
13. Olson LG, Bathe KJ. Analysis of fluid–structure interactions—a direct symmetric coupled formulation based on the fluid velocity potential. *Computers and Structures* 1985; **21**(1–2):21–32.
14. Wang XD, Bathe KJ. Displacement pressure based mixed finite element formulations for acoustic fluid–structure interaction problems. *International Journal for Numerical Methods in Engineering* 1997; **40**(11):2001–2017.
15. Wilson EL, Khalvati M. Finite-elements for the dynamic analysis of fluid–solid systems. *International Journal for Numerical Methods in Engineering* 1983; **19**(11):1657–1668.
16. Chen HC, Taylor RL. Vibration analysis of fluid solid systems using a finite-element displacement formulation. *International Journal for Numerical Methods in Engineering* 1990; **29**(4):683–698.




DOI: 10.1002/nme

17. Gopalakrishnan S. Behaviour of isoparametric quadrilateral family of Lagrangian fluid finite elements. *International Journal for Numerical Methods in Engineering* 2002; **54**(5):731–761.
18. Park KC, Underwood PG. A variable-step central difference method for structural dynamics analysis. 1. Theoretical aspects. *Computer Methods in Applied Mechanics and Engineering* 1980; **22**(2):241–258.
19. Krysl P, Belytschko T. Object-oriented parallelization of explicit structural dynamics with PVM. *Computers and Structures* 1998; **66**(2–3):259–273.
20. Hughes TJR. *The Finite Element Method. Linear Static and Dynamic Finite Element Analysis*. Dover publications: New York, 2000.
21. Felippa CA. A family of early-time approximations for fluid–structure interaction. *Journal of Applied Mechanics—Transactions of the ASME* 1980; **47**(4):703–708.
22. Pinsky PM, Abboud NN. Finite-element solution of the transient exterior structural acoustics problem based on the use of radially asymptotic boundary operators. *Computer Methods in Applied Mechanics and Engineering* 1991; **85**(3):311–348.
23. Kallivokas LF, Bielak J. Time-domain analysis of transient structural acoustics problems based on the finite-element method and a novel absorbing boundary-element. *Journal of the Acoustical Society of America* 1993; **94**(6):3480–3492.
24. Thompson LL, Huan RN. Computation of far-field solutions based on exact nonreflecting boundary conditions for the time-dependent wave equation. *Computer Methods in Applied Mechanics and Engineering* 2000; **190**(11–12): 1551–1577.
25. Tezaur R, Macedo A, Farhat C, Djellouli R. Three-dimensional finite element calculations in acoustic scattering using arbitrarily shaped convex artificial boundaries. *International Journal for Numerical Methods in Engineering* 2002; **53**(6):1461–1476.
26. Reiner RC, Djellouli R. Improvement of the performance of the BGT2 condition for low frequency acoustic scattering problems. *Wave Motion* 2006; **43**(5):406–424.
27. Mindlin RD, Bleich HH. Response of an elastic cylindrical shell to a transverse, step shockwave. *Journal of Applied Mechanics—Transactions of the ASME* 1953; **20**:189–195.
28. Haywood JH. Response of an elastic cylindrical shell to a transverse, step shockwave. *Journal of Mechanics and Applied Mathematics* 1958; **11**:129–141.
29. Geers TL, Felippa CA. Doubly asymptotic approximations for vibration analysis of submerged structures. *Journal of the Acoustical Society of America* 1983; **73**(4):1152–1159.
30. Huang H. An exact analysis of the transient interaction of acoustic plane waves with a cylindrical elastic shell. *Journal of Applied Mechanics—Transactions of the ASME* 1970; **37**:1091–1099.
31. Zilliacus S. Fluid–structure interaction and ADINA. *Computers and Structures* 1983; **17**(5–6):763–773.
32. Hamdan FH. Near-field fluid–structure interaction using Lagrangian fluid finite elements. *Computers and Structures* 1999; **71**(2):123–141.
33. Fan SC, Wang K, Yu GY, Lie ST. Spline shell element and plane-wave approximation for dynamic response of submerged structures. *Computers and Structures* 2001; **79**(18):1635–1644.
34. Lie ST, Yu GY, Zhao Z. Coupling of BEM/FEM for time domain structural–acoustic interaction problems. *CMES—Computer Modeling in Engineering and Sciences* 2001; **2**(2):171–180.
35. Lie ST, Yu G. Multi-domain fluid–structure interaction analysis with a stable time domain BEM/FEM coupling procedure. *Engineering Computations* 2002; **19**(1–2):6–21.
36. Yu GY. Symmetric collocation BEM/FEM coupling procedure for 2-d dynamic structural–acoustic interaction problems. *Computational Mechanics* 2002; **29**:191–198.
37. Dohrmann CR, Heinstein MW, Jung J, Key SW, Witkowski WW. Node-based uniform strain elements for three-node triangular and four-node tetrahedral meshes. *International Journal for Numerical Methods in Engineering* 2000; **47**:1549–1568.
38. Krysl P, Zhu B. Locking-free continuum displacement finite elements with nodal integration, 2007, in preparation.
39. Lee YT, Requicha AAG. Algorithms for computing the volume and other integral properties of solids. 1. Known methods and open issues. *Communications of the ACM* 1982; **25**(9):635–641.
40. Hollister SJ, Kikuchi N. Homogenization theory and digital imaging—a basis for studying the mechanics and design principles of bone tissue. *Biotechnology and Bioengineering* 1994; **43**(7):586–596.
41. Terada K, Miura T, Kikuchi N. Digital image-based modeling applied to the homogenization analysis of composite materials. *Computational Mechanics* 1997; **20**(4):331–346.
42. Koketsu K, Fujiwara H, Ikegami Y. Finite-element simulation of seismic ground motion with a voxel mesh. *Pure and Applied Geophysics* 2004; **161**(11–12):2183–2198.



DOI: 10.1002/nme

43. Krysl P, Cranford TW, Wiggins SM, Hildebrand JA. Simulating the effect of high-intensity sound on cetaceans: modeling, approach and a case study for Cuvier's beaked whale (*Ziphius cavirostris*). *Journal of the Acoustical Society of America* 2006; **120**(4):2328–2339.
44. Soldevilla MS, Mckenna ME, Wiggins SM, Shadwick RE, Cranford TW, Hildebrand JA. Cuvier's beaked whale (Ziphius cavirostris) head tissues: physical properties and CT imaging. *Journal Of Experimental Biology* 2005; **208**(12):2319–2332.
45. Taylor RL, Beresford PJ, Wilson EL. Non-conforming element for stress analysis. *International Journal for Numerical Methods in Engineering* 1976; **10**(6):1211–1219.
46. Kitware Inc, http://public.kitware.com/VTK/. *VTK*: *The visualization toolkit*, 2007.
47. Morse PM, Ingard KU. *Theoretical Acoustics*. Princeton University Press: Princeton, NJ, 1968.
48. O'Brien WD. Evaluation of acoustic propagation paths into the human head. *Technical Report AFRL-SR-AR-TR-05-0349*, Air Force office of scientific research, 2005.
49. Raichel DR. *The Science and Applications of Acoustics* (2nd edn). Springer: Berlin, 2006.
50. Koike T, Wada H, Kobayashi T. Modeling of the human middle ear using the finite-element method. *Journal of the Acoustical Society of America* 2002; **111**(3):1306–1317.
51. Stenfelt S, Hato N, Goode RL. Fluid volume displacement at the oval and round windows with air and bone conduction stimulation. *Journal of the Acoustical Society of America* 2004; **115**(2):797–812.
52. Stenfelt S. Middle ear ossicles motion at hearing thresholds with air conduction and bone conduction stimulation. *Journal of the Acoustical Society of America* 2006; **119**(5):2848–2858.
53. Bohnke F, Arnold W. Bone conduction in a three-dimensional model of the cochlea. *ORL—Journal for Oto-Rhino-Laryngology and its Related Specialties* 2006; **68**(6):393–396.
54. Taschke H, Hudde H. A finite element model of the human head for auditory bone conduction simulation. *ORL—Journal for Oto-Rhino-Laryngology and its Related Specialties* 2006; **68**(6):319–323.
55. Aroyan JL. Three-dimensional modeling of hearing in *Delphinus delphis*. *Journal of the Acoustical Society of America* 2001; **110**(6):3305–3318.
56. Zimmer WMX, Johnson MP, Madsen PT, Tyack PL. Echolocation clicks of free-ranging Cuvier's beaked whales (*Ziphius cavirostris*). *Journal of the Acoustical Society of America* 2005; **117**(6):3919–3927.
57. Au WWL, Kastelein RA, Benoit-Bird KJ, Cranford TW, Mckenna MF. Acoustic radiation from the head of echolocating harbor porpoises (*Phocoena phocoena*). *Journal Of Experimental Biology* 2006; **209**(14):2726–2733.
58. Sarvazyan A. Model-based imaging. *Ultrasound in Medicine and Biology* 2006; **32**(11):1713–1720.
59. Berry GP, Bamber JC, Armstrong CG, Miller NR, Barbone PE. Towards an acoustic model-based poroelastic imaging method: I. Theoretical foundation. *Ultrasound in Medicine and Biology* 2006; **32**(4):547–567.
60. O'Brien WD. Ultrasound-biophysics mechanisms. *Progress in Biophysics and Molecular Biology* 2007; **93**(1–3): 212–255.



DOI: 10.1002/nme